Gradient self-doped $CuBi_2O_4$ with highly improved charge separation efficiency

Fuxian Wang[1], Wilman Septina[2], Abdelkrim Chemseddine[1], Fatwa F. Abdi[1], Dennis Friedrich[1], Peter Bogdanoff[1], Roel van de Krol[1], S. David Tilley[2], Sean P. Berglund[1*]

[1]Helmholtz-Zentrum Berlin für Materialien und Energie GmbH, Institute for Solar Fuels, Hahn-Meitner-Platz 1, 14109 Berlin, Germany

[2]Department of Chemistry, University of Zurich, Winterthurerstrasse 190, CH-8057 Zurich, Switzerland

KEYWORDS: water splitting, $CuBi_2O_4$, gradient doping, charge separation efficiency, protection layers, H_2 production, spray pyrolysis.

ABSTRACT: A new strategy of using forward gradient self-doping to improve the charge separation efficiency in metal oxide photoelectrodes is proposed. Gradient self-doped $CuBi_2O_4$ photocathodes are prepared with forward and reverse gradients in copper vacancies using a two-step, diffusion-assisted spray pyrolysis process. Decreasing the Cu/Bi ratio of the $CuBi_2O_4$ photocathodes introduces Cu vacancies that increase the carrier (hole) concentration and lowers the Fermi level, as evidenced by a shift in the flat-band toward more positive potentials. Thus a gradient in Cu vacancies leads to an internal electric-field within $CuBi_2O_4$, which can facilitate charge separation. Compared to homogeneous $CuBi_2O_4$ photocathodes, $CuBi_2O_4$ photocathodes with a forward gradient show highly improved charge separation efficiency and enhanced photoelectrochemical performance for reduction reactions, while $CuBi_2O_4$ photocathodes with a reverse gradient show significantly reduced charge separation efficiency and photoelectrochemical performance. The $CuBi_2O_4$ photocathodes with a forward gradient produce record AM 1.5 photocurrent densities for $CuBi_2O_4$ up to -2.5 mA/cm^2 at 0.6 V vs. RHE with H_2O_2 as an electron scavenger and they show a charge separation efficiency of 34 % for 550 nm light. The gradient self-doping accomplishes this without the introduction of external dopants and therefore the tetragonal crystal structure and carrier mobility of $CuBi_2O_4$ are maintained. Lastly, forward gradient self-doped $CuBi_2O_4$ photocathodes are protected with a CdS/TiO_2 heterojunction and coated with Pt as an electrocatalyst. These photocathodes demonstrate photocurrent densities on the order of -1.0 mA/cm^2 at 0.0 V vs. RHE and evolve hydrogen with a faradaic efficiency of ~91 %.

INTRODUCTION

$CuBi_2O_4$, a p-type semiconductor, has attracted attention as a photocathode material for solar water splitting due to its attractive material properties. First, it has a suitable band gap in the range of 1.5-1.8 eV so it can utilize a significant portion of the visible light from the solar spectrum.[1-4] Second, its conduction band is located at a more negative potential than the reduction potential of H^+/H_2, allowing for solar H_2 production.[5-7] Third, its valence band lies at more positive potentials than that of other photocathode materials, such as Cu-based metal oxides, p-Si, and p-GaP, and it shows an unusually positive photocurrent onset potential near +1 V vs. RHE. This implies that the material is able to generate a relatively large internal photovoltage.[3] Theoretically, $CuBi_2O_4$ can generate a maximum AM1.5 photocurrent density of 19.7–29.0 mA/cm^2, assuming all photons with energies higher than the bandgap are absorbed and utilized with 100 % efficiency.[8] However, the experimental photocurrent densities reported so far have been well below this theoretical maximum.[1-3, 9] Our recent work demonstrated that the photoelectrochemical (PEC) performance is largely limited by poor charge separation and transport in the bulk of the material as well as photo-corrosion in aqueous solutions.[4]

One way to improve the charge separation of a semiconductor material is to create a built-in electric field. This is commonly accomplished by using a heterojunction, in which direct contact between two different semiconductors results in a re-distribution of charge carriers and, therefore, band bending within the depletion region. To create an effective heterojunction, specific constraints must be met. The two semiconductors must have suitably aligned energy levels, and they must be synthesized in a manner that results in good interfacial contact[10-12].

Specifically, the formation of defects at the interface needs to be avoided, as this can lead to high level of recombination[13].

An alternative approach to creating an internal electric field is by using a homojunction, in which the same semiconductors with equal bandgaps but different doping levels are placed in contact. A p-n silicon solar cell is an example of a homojunction photovoltaic device. Photoelectrodes can also be synthesized as homojunctions. For example, it has been demonstrated that W : $BiVO_4$ photoanodes with a gradient in the W doping level possess an internal electric field, which significantly enhances the charge separation efficiency[14]. Compared to heterojunctions, homojunctions are usually easier to prepare since they only require a single semiconductor material. However, one limitation of gradient doped homojunctions is that the addition of an external dopant can create recombination centers and decrease the charge carrier mobility and lifetime. It has been demonstrated this in some detail for W doped $BiVO_4$[15, 16]. Moreover, the external dopant can add to the complexity of the synthesis process.

In this work, we show a new approach for creating effective homojunctions within photoelectrodes composed of multinary metal oxides like $CuBi_2O_4$ without the addition of an external dopant. According to DFT calculations,[6] $CuBi_2O_4$ has a conduction band (CB) and valence band (VB) arising primarily from the Cu 3d and O 2p orbitals, respectively. Copper vacancies (denoted as V''_{Cu}) are the energetically most probable defects in $CuBi_2O_4$. These native defects are presumably charge-compensated by free holes, which shift the Fermi level closer to the valence band and cause the p-type behavior of $CuBi_2O_4$. This suggests that the Fermi level energy of $CuBi_2O_4$ can be tailored by varying the concentration of V''_{Cu}. We have taken advantage of this principle and developed a synthesis procedure that results in a V''_{Cu} gradient within $CuBi_2O_4$ and hence a gradient in the Fermi level and a built-in electric field without the introduction of an external dopant. $CuBi_2O_4$ photocathodes synthesized with a forward gradient (i.e., Cu/Bi atomic ratio gradually increasing from the substrate to the surface of the film) show significantly enhanced charge separation efficiency compared to photocathodes without a gradient or a reverse gradient. To the best of our knowledge, this concept of using gradient self-doping to create an internal electric field in a multinary metal oxide photoelectrode has not previously been reported.

Lastly, we address the limitation of photo-corrosion by depositing a CdS/TiO_2 heterojunction layer on top of the forward gradient $CuBi_2O_4$ photocathodes along with Pt as an electrocatalyst. This dramatically improves the stability of the $CuBi_2O_4$ photocathodes in aqueous electrolyte. In addition photoelectrochemical H_2 production is confirmed.

RESULTS AND DISCUSSION

Photoelectrochemical performance and optical properties

Figure 1a shows a chopped linear sweep voltammetry (LSV) scan for three different $CuBi_2O_4$ photocathodes synthesized with a uniform $CuBi_2O_4$ composition (homogeneous) or with gradient self-doping (forward and reverse). H_2O_2 was added to the electrolyte as an electron scavenger to test the $CuBi_2O_4$ photocathodes without limitations in the reaction kinetics, which would be the case for proton reduction. The homogeneous $CuBi_2O_4$ photocathodes were prepared using our previously reported recipe,[4] while the gradient self-doped $CuBi_2O_4$ photocathodes were fabricated using a two-step diffusion-assisted spray pyrolysis process. Briefly, photocathodes with a forward gradient were prepared by first spraying the Bi precursor solution onto heated FTO (F: SnO_2) substrates, followed by spraying of the Cu precursor solution. For the reverse gradients, the spray order was reversed. The high mobility of the Cu atoms resulted in rapid diffusion and the formation of crystalline $CuBi_2O_4$ films (*vide infra*). More details on the synthesis can be found in the experimental section.

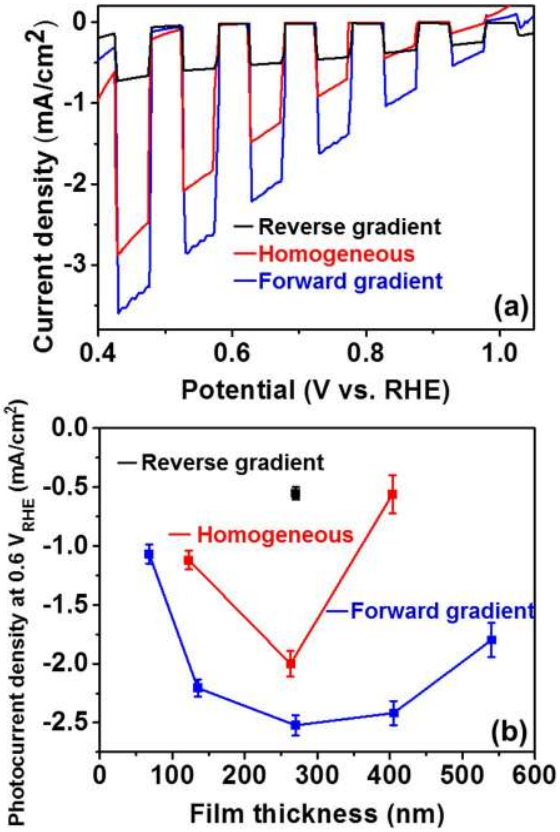

Figure 1. (a) chopped LSV scans for $CuBi_2O_4$ photocathodes synthesized to a thickness of ~ 270 nm with uniform composition (homogeneous) or with gradient self-doping (forward and reverse) (b) Average photocurrent densities at 0.6 V vs. RHE as a function of film thickness extracted from LSV scans (see Figure S1 for LSV scans). The measurements were performed in 0.3 M K_2SO_4 and 0.2 M phosphate buffer (pH 6.65) with H_2O_2 under back illumination.

For Figure 1a, all three photocathodes were synthesized to a $CuBi_2O_4$ thickness of ~ 270 nm. Clearly, the $CuBi_2O_4$ photocathode with the forward gradient shows a higher photocurrent than both the homogeneous and reverse gradient photocathode. This remains true for a wide range of $CuBi_2O_4$ film thicknesses, as illustrated in Figure 1b where the photocurrent densities at 0.6 V vs. RHE were extracted from LSV measurements and plotted as a function of the $CuBi_2O_4$ film thickness. $CuBi_2O_4$ photocathodes with a reverse gradient were only tested at one thickness but produced substantially lower photocurrent than the other photocathodes. At 0.6 V vs. RHE the ~270 nm $CuBi_2O_4$ photocathodes with the forward gradient produce an average photocurrent density of -2.5 mA/cm^2, which is 25 % higher than the -2.0 mA/cm^2 of the homogeneous $CuBi_2O_4$ photocathodes, and establishes a new benchmark for this material.[3-4, 9, 17] For the forward gradient film, back illumination produces higher photocurrent than front-side illumination, as shown in Figure S2.

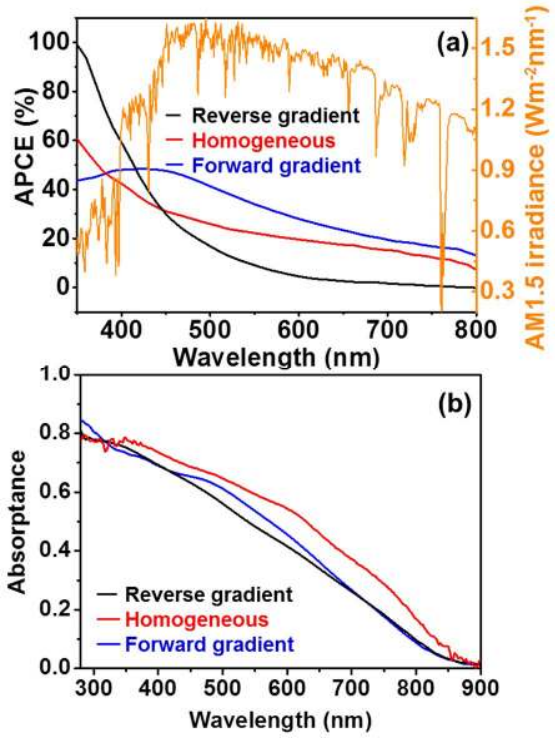

Figure 2. (a) APCE spectra for different $CuBi_2O_4$ photocathodes along with the AM 1.5 irradiance spectrum, (b) Absorption spectra for different $CuBi_2O_4$ films, each has a thickness of ~ 270 nm.

The quantum efficiency of each $CuBi_2O_4$ photocathode was determined by measuring the incident photon-to-current efficiency (IPCE) and absorbed photon-to-current efficiency (APCE). Figure 2a shows the APCE spectra for each photocathode measured at 0.6 V vs. RHE under back illumination. For the most intense region of the AM 1.5 solar spectrum, 390 to 800 nm, the $CuBi_2O_4$ photocathode with a forward gradient shows significantly higher APCE than the homogeneous $CuBi_2O_4$ photocathode, which is consistent with the overall PEC performance. In contrast, the $CuBi_2O_4$ photocathode with a reverse gradient exhibits a significantly lower APCE than the homogeneous $CuBi_2O_4$ photocathode for wavelengths above 420 nm. The APCE values were calculated using the IPCE data in Figures S3, S4, and S5 and the absorptance spectra shown in Figure 2b. No significant difference in absorptance was observed among the different $CuBi_2O_4$ films. In fact the $CuBi_2O_4$ photocathode with a forward gradient shows slightly lower absorptance than the homogeneous $CuBi_2O_4$ photocathode. This proves that the higher IPCE for the forward gradient $CuBi_2O_4$ is not due to differences in the absorptance of the sample. Since the IPCE/APCE measurements were also done in the presence of H_2O_2, the injection efficiency can be assumed to be 100 % and, therefore, the APCE represents the charge separation efficiency. At 550 nm, the APCE values are 34 %, 22 % and 9 % for the forward gradient, homogeneous, and reverse gradient $CuBi_2O_4$ photocathodes, respectively. Thus, the forward gradient indeed improves the charge separation efficiency while the reverse gradient impedes it. For short wavelengths (≤420 nm), the APCEs of homogeneous and reverse gradient films are actually higher than that of the forward gradient films. One possible explanation for this is that the higher energy, shorter wavelength photons generate more electron-hole pairs near the FTO/$CuBi_2O_4$ interface (due to the high absorption coefficient). For the forward gradient films, this region has a higher concentration of Cu vacancies (*vide infra*) and consequently a higher recombination rate. Whereas electron-hole pairs generated further into the $CuBi_2O_4$ film by lower energy light are more efficiently separated by the internal electric-field.

We note that when H_2O_2 is used as an electron scavenger for photoelectrochemical tests, current doubling is possible. To try to exclude the possibility of current doubling we tested the $CuBi_2O_4$ photocathodes in other kinetically facile redox couples as well, including $FeCl_2/FeCl_3$ (Fe^{2+}/Fe^{3+}) and NaI/I_2 ($3I^-/I_3^-$) in acetonitrile. Unfortunately, $FeCl_2/FeCl_3$ resulted in extremely high dark currents at potentials more negative than 0.6 V vs. NHE (Figure S6) and NaI/I_2 produced large transient spikes in the photocurrent (Figure S7), presumably due to recombination or back reactions at the photocathode surface.[18-19] We therefore conclude that $FeCl_2/FeCl_3$ and NaI/I_2 were not effective electron scavengers for our $CuBi_2O_4$. In our previous study we tested homogeneous $CuBi_2O_4$ photocathodes in KOH with O_2 bubbling as an electron scavenger; however O_2 also has the possibility of current doubling at low light intensities and transient spikes in photocurrent were observed.[4, 20] Of all the electron scavengers that we tested, H_2O_2 was the only one that completely eliminated the transient spikes in photo-

current and prevented high dark current thereby allowing us to probe the charge separation efficiency within the $CuBi_2O_4$ films.

Crystal structure and electronic properties

To check the crystal structure and phase composition of the different $CuBi_2O_4$ films, X-ray diffraction (XRD) and Raman analysis were performed. Figure 3a shows the X-ray diffractograms of the forward gradient, homogeneous, and reverse gradient $CuBi_2O_4$ films on FTO substrates. The JCPDS reference pattern for SnO_2 (PDF # 00-046-1088) is indicated with green bars and tetragonal $CuBi_2O_4$ (PDF # 42-0334) is indicated with pink bars. All $CuBi_2O_4$ films show strong peaks at 20.88 °, 28.01 °, and 46.7 °, which can be assigned to the (200), (211), and (411) lattice planes of tetragonal $CuBi_2O_4$, respectively. For the homogeneous and forward gradient $CuBi_2O_4$ films, two additional peaks are visible at 35.44 ° and 38.68 °. These two peaks can be assigned to the (002) and (111) reflexes of monoclinic CuO (PDF# 48-1548), respectively. This may arise due to premature thermal decomposition of $Cu(NO_3)_2 \cdot 3H_2O$ in the precursor solution to CuO, which can occur at temperatures as low as 310 °C.[21] The presence of Bi_2O_3 was not revealed by the XRD data in Figure 3a. However, we cannot exclude the possibility that the Bi_2O_3 peaks are obscured due to the strong similarity of the diffractograms of Bi_2O_3 and $CuBi_2O_4$, or to the absence of long-range order in an amorphous or nanocrystalline Bi_2O_3 phase that has segregated at the grain boundaries. Scherrer analysis of the XRD patterns reveals that the $CuBi_2O_4$ films with forward and reverse gradients have similar crystallite sizes of 35.7 nm and 38.2 nm respectively (see Figures S8 and S9).

Figure 3b shows the Raman spectrums of the different $CuBi_2O_4$ samples. The main Raman bands for $CuBi_2O_4$ centered at 126, 261, 405, and 577 cm^{-1} were observed for all films. The assignment of these bands can be found in the literature.[22-23] The existence of CuO was also confirmed by the appearance of two additional peaks at ~296 and 344 cm^{-1}, which correspond to the A_g and B_g vibration modes of CuO, respectively.[24] No Raman peaks for Bi_2O_3 are observed, which is consistent with the XRD results.

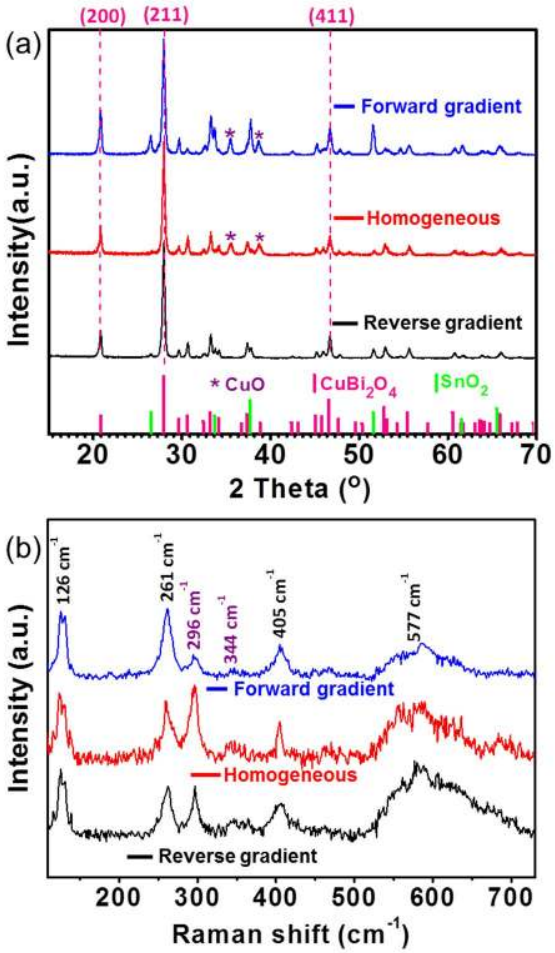

Figure 3. (a) XRD diffractograms and (b) Raman spectrums for forward gradient, homogeneous, and reverse gradient $CuBi_2O_4$ photocathodes with a thickness of ~ 270 nm.

The $CuBi_2O_4$ film morphologies and elemental composition were characterized using scanning electron microscopy (SEM) along with energy dispersive X-ray (EDX) spectroscopy. Figures 4a, 4b, and 4c show cross-sectional SEM images of the forward gradient, homogeneous, and reverse gradient $CuBi_2O_4$ thin films, respectively. As previously reported the homogeneous $CuBi_2O_4$ film has a highly dense and compact morphology.[4] The forward gradient film has a less uniform morphology due to the bottom layer of larger Bi-rich particles being coated with smaller Cu-rich particles. The reverse gradient film shows the opposite with a thin Cu-rich bottom layer being covered by larger, asymmetrical Bi-rich particles. This was confirmed by EDX mapping of the cross-sections, which is described below. The porosity, particle size, and surface roughness of thin film photoelectrodes are known to influence the charge carrier transport.[25] For instance, a higher porosity allows electrolyte to penetrate deeper into the film making it easier for the minority charge carriers to reach the electrolyte. In order to quantify the surface roughness, atomic force microscopy (AFM) was performed on homogeneous and forward gradient, homogeneous, and reverse gradient films, as shown in Figure S10. The reverse gradient showed the highest surface roughness but the lowest photocurrent density by a significant amount, so the specific surface area of the film is not the main determinant in photoactivity. This is as expected, since we avoided any kinetic limitations in the electrochemical reaction by adding H_2O_2 as an electron scavenger.

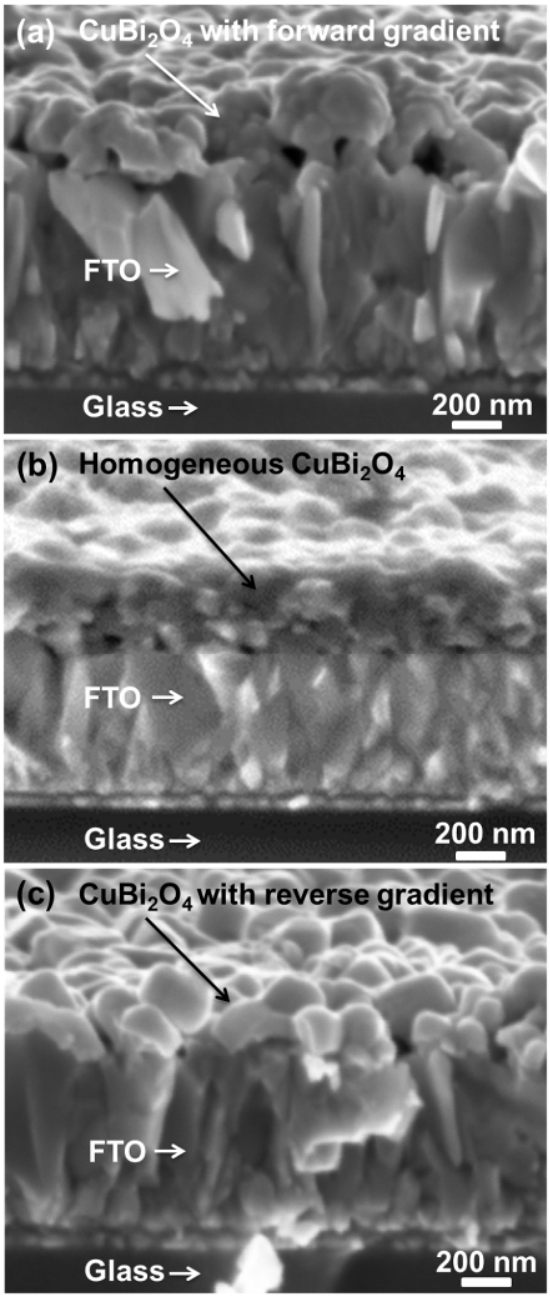

Figure 4. SEM images of ~ 270 nm $CuBi_2O_4$ thin films (a) with forward gradient, (b) without gradient (homogeneous), and (c) with reverse gradient.

Figure 5 shows a cross-section SEM image of a forward gradient $CuBi_2O_4$ photocathode with EDX mapping overlaid. The elements Sn, Cu, and Bi are indicated by the colors yellow, red, and cyan respectively. From the EDX mapping it is clear that the top of the film has a higher Cu concentration while the Bi concentration is higher next to the FTO.

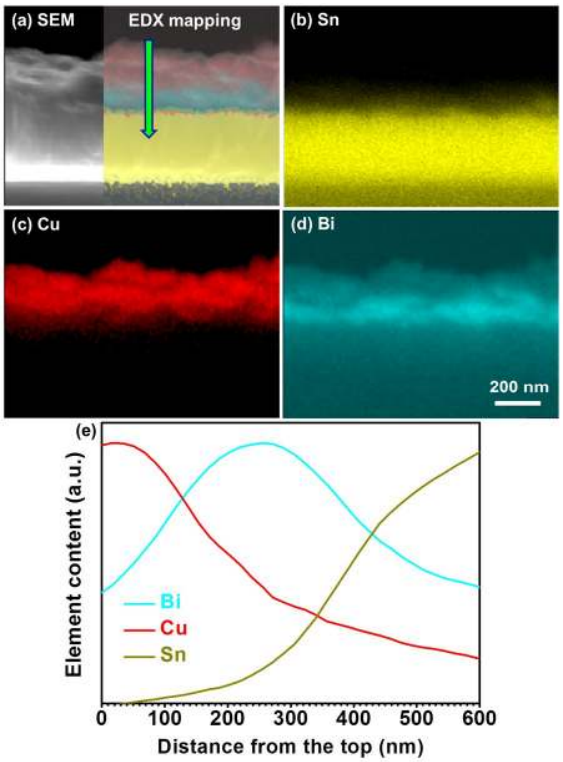

Figure 5. (a) SEM image with EDX mapping overlaid, (b) Sn distribution, (c) Cu distribution, (d) Bi distribution, and (e) linear scan of each elemental distribution in the direction of the green arrow for a forward gradient $CuBi_2O_4$ photocathode.

A linear scan of the EDX mapping was performed in the direction indicated by the green arrow in Figure 5a and the element count was plotted in Figure 5e. This confirms that a gradient in the Cu/Bi ratio is truly present within the forward gradient $CuBi_2O_4$ photocathode. EDX mapping was also used to verify a gradient in the Cu/Bi ratio in the opposite direction for the reverse gradient photocathode (see Figure S11). Although not as obvious as in the forward gradient film, the Cu/Bi ratio at the surface of the reverse gradient film is clearly lower than the Cu/Bi ratio deeper in the film. This is probably due to the different film formation mechanisms. In the forward gradient, copper is deposited on Bi_2O_3 which can be seen as host structure for the small copper ions. In this case the film does not go through dramatic structural and morphological changes. In the reverse gradient, the original CuO needs to be breaken down in order to form $CuBi_2O_4$.(from Karim)

In order to investigate how the Cu/Bi ratio affects the Fermi level and valence band edge of $CuBi_2O_4$, we prepared homogeneous $CuBi_2O_4$ films with different stoichiometries using our previously reported optimized spray pyrolysis recipe.[4] The stoichiometries were (a) Cu/Bi = 1/3, Cu-deficient $CuBi_2O_4$, (b) Cu/Bi = 1/2, stoichiometric $CuBi_2O_4$, and (c) Cu/Bi = 1/ 1, Cu-rich $CuBi_2O_4$. XRD measurements confirmed that the tetragonal crystal structure was maintained even for

Table 1. Summary of the ϕ_{fb} and N_A for ~270 nm $CuBi_2O_4$ films with different Cu/Bi ratios.

$CuBi_2O_4$ film	Cu/Bi ratio	ϕ_{fb} (V vs. RHE)	N_A (cm^{-3})
Cu-deficient $CuBi_2O_4$	1/3	1.25 ± 0.02	~7.3×10^{19}
Stoichiometric $CuBi_2O_4$	1/2	1.21 ± 0.01	~7.6×10^{18}
Cu-rich $CuBi_2O_4$	1/1	1.09 ± 0.02	~6.9×10^{18}

the non-stoichiometric $CuBi_2O_4$ films, as shown in Figure S12. The surface area of each film was estimated by atomic force microscopy (AFM) and Mott-Schottky measurements were performed as shown in Figures S13, S14, and S15. Dark cyclic voltammetry tests were carried out in the same potential range as Mott-Schottky measurements to confirm that corrosion did not occur. As shown in Figure S16, no cathodic current was observed in this potential range, indicating no reduction of Cu^{2+}. The flat-band potential (φ_{fb}) was determined from the extrapolated x-axis intercepts of Mott-Schottky plots and the acceptor density (N_A) was calculated from the slopes. The results are summarized in Table 1 and show that when the Cu/Bi ratio decreases, the φ_{fb} shifts to more positive potentials. This means that the Fermi level shifts toward the valence band edge (Figure. 6a). This is consistent with our assumption that Cu vacancies are charge-compensated by free holes, and that the Fermi level can be tailored simply by controlling the concentration of Cu vacancies, $[V''_{Cu}]$.

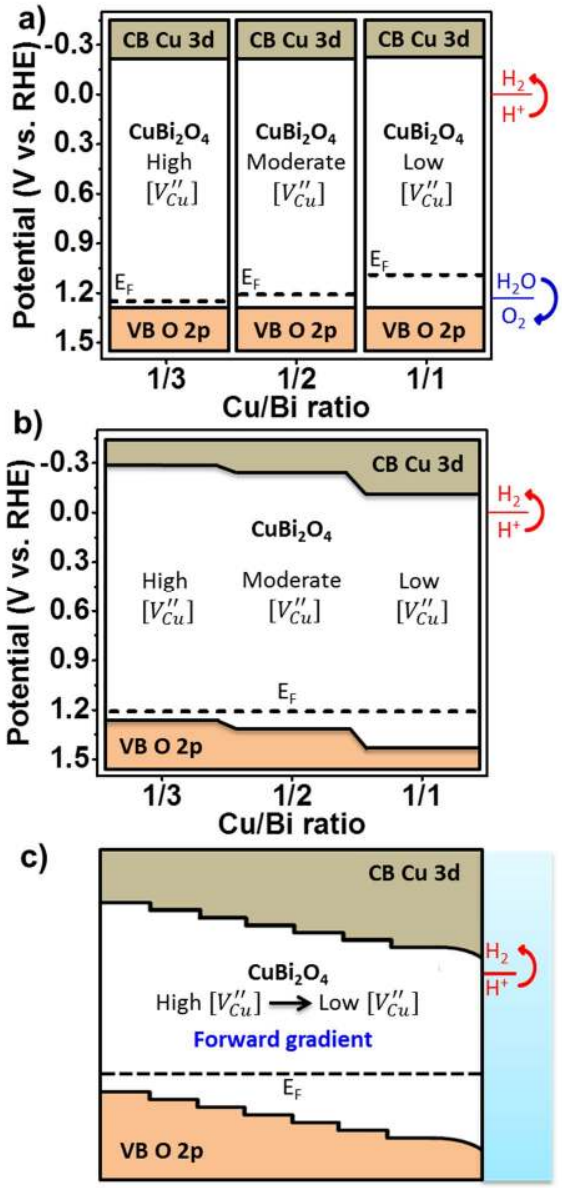

Figure 6. (a) flat-band potential of homogeneous $CuBi_2O_4$ films with different stoichiometries, (b) the formation of a $CuBi_2O_4$ homojunction when brought in to contact, (c) the formation of $CuBi_2O_4$ with forward gradient.

Figure 6 illustrates how a gradient in $[V''_{Cu}]$ and the resulting gradient in the Fermi level leads to an internal electric field. Before contact, $CuBi_2O_4$ films with different Cu/Bi ratios will possess different Fermi levels as shown in Figure 6a. After contact, the Fermi levels will equilibrate by distributing the free carriers between the different regions, so that the CB and VB bend at each interface as illustrated by Figure 6b. A forward gradient $CuBi_2O_4$ photocathode will contain the band bending shown in Figure 6c, which would promote charge separation by field-enhanced diffusion (drift) of the photo-generated electrons towards the $CuBi_2O_4$-electrolyte interface and drift of photo-generated holes towards the back contact.

The carrier transport and recombination properties of the different $CuBi_2O_4$ films were investigated using time resolved microwave conductivity (TRMC) measurements. The TRMC signal decays for a forward gradient, homogeneous, and reverse gradient are shown in Figure 7.

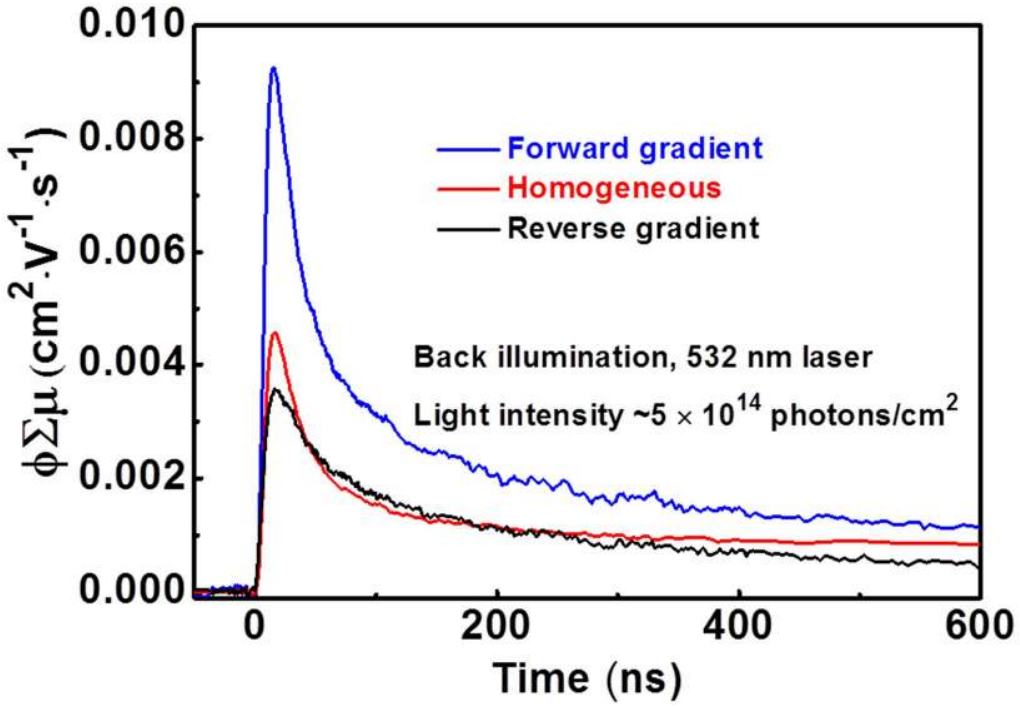

Figure 7. TRMC signal for ~270 nm $CuBi_2O_4$ films deposited on quartz substrates (a) with a forward gradient, (b) without a gradient (homogeneous), and (c) with a reverse gradient.

The charge carrier mobilities (μ) were extracted from the peak TRMC signals ($\phi\Sigma\mu_{max}$), while the charge carrier lifetimes were deduced from the decay of the curve. All three curves showed two distinct time constants, τ_1 and τ_2. The corresponding diffusion lengths were calculated from the charge carrier mobilities and lifetimes. These values are summarized in Table 2, details of the fitting can be found in Figure S17 and Table S1.

Table 2. Summary of the charge carrier mobility, $\phi\Sigma\mu_{max}$, time constants, τ_1 and τ_2 , and the corresponding diffusion lengths, L_{D1} and L_{D2}. The error estimates reflect the spread in the measured values for different samples.

$CuBi_2O_4$ film	$\phi\Sigma\mu_{max}$ ($10^{-3} cm^2 V^{-1} s^{-1}$)	τ_1 (ns)	τ_2 (ns)	L_{D1} (nm)	L_{D2} (nm)
Forward gradient	9.3 ± 2.2	20.2 ± 3.6	142.6 ± 5.5	20.6 ± 0.2	60.0 ± 2.5
Homogeneous	4.6 ± 0.7	22.7 ± 0.7	153.0 ± 10.4	16.3 ± 0.3	42.4 ± 1.5
Reverse gradient	3.6 ± 0.8	35.0 ± 1.3	237.2 ± 6.3	16.9 ± 1.5	43.9 ± 3.5

The μ values for the various $CuBi_2O_4$ films were all of the same order of magnitude at 0.007, 0.005, and 0.003 $cm^2 V^{-1} s^{-1}$ for the forward gradient, homogeneous, and reverse gradient films respectively. This result for self-doping is in sharp contrast to the significant decrease (20 times) in mobility observed when W was incorporated into $BiVO_4$ as an external dopant.[15-16] Similar to $CuBi_2O_4$ films synthesized by drop-casting,[3] the $CuBi_2O_4$ films synthesized by spray-pyrolysis for this study show two different lifetimes and corresponding diffusion lengths. The L_{D1}/L_{D2} values are 21 nm/60 nm, 16 nm/42 nm, and 17 nm/44 nm for the forward gradient, homogeneous, and reverse gradient films, respectively.

The charge carrier diffusion length is a key parameter in determining the PEC performance of a material. Indeed the forward gradient $CuBi_2O_4$ film shows the longest charge carrier diffusion lengths and the highest photocurrent density (see Figure 1). However the charge carrier diffusion lengths for the forward gradient film are only 1.3 to 1.5 times larger than those for the reverse gradient films while the photocurrent density is 5 times larger. From this, we conclude that the observed improvement in photoactivity is mainly due to the internal band bending induced by the forward gradient in $[V''_{Cu}]$.

We finally note that although the Cu sub-stoichiometry in our films can be used as a proxy for $[V''_{Cu}]$ (since Cu vancancies are known to be the dominant defects in $CuBi_2O_4$), direct observation of a gradient in $[V''_{Cu}]$ would

allow one to further quantify the relationship between these defects and the photoactivity of the material. Cu vacancies can be directly observed with a technique like positron annihiliation spectroscopy. Showing the presence of a $[V''_{Cu}]$ gradient across the thickness of a $CuBi_2O_4$ film, however, would pose a significant experimental challenge.

Photoelectrochemical stability and H_2 production

Ultimately, the goal is to utilize $CuBi_2O_4$ as a material for solar water splitting, so the forward gradient $CuBi_2O_4$ photocathodes should be tested under water splitting conditions without an electron scavenger. Unfortunately many Cu-based metal oxides, including Cu_2O, CuO, and $CuBi_2O_4$, are highly susceptible to photo-corrosion when illuminated in aqueous solutions.[26] This is also the case for our forward gradient $CuBi_2O_4$ films, as confirmed by the chopped LSV scan performed in pH neutral electrolyte with Ar bubbling, which is shown in Figure S18. At potentials more negative than 0.4 V vs. RHE the $CuBi_2O_4$ photocathode shows a rapid increase in dark current due to electrochemical corrosion. Based on previous reports, the Cu^{2+} in $CuBi_2O_4$ is most likely reduced to Cu^{1+} and Cu.[3-4]

One recently developed strategy for preventing photo-corrosion in photoelectrodes is the application of protection layers such as TiO_2, which can be deposited conformally using atomic layer deposition (ALD).[27-29] Recently, CuO photocathodes were effectively protected by first adding a layer of CdS using chemical bath deposition followed by ALD of TiO_2 and photo-electrochemical deposition of Pt as an electrocatalyst.[30] The resulting $CuO/CdS/TiO_2/Pt$ heterojunction photocathodes produced photocurrent densities greater than -1 mA/cm^2 at 0.0 V vs. RHE with a Faradaic efficiency of nearly 100 % for H_2 production. Here we adopt this CdS/TiO_2 heterojunction strategy to the forward gradient $CuBi_2O_4$ photocathodes to assess their ability to produce hydrogen. Figure S19 shows the cross section SEM image of the forward gradient $CuBi_2O_4/CdS/TiO_2/Pt$ photocathode.

Figure 8a shows the chopped LSV for the forward gradient $CuBi_2O_4/CdS/TiO_2/Pt$ photocathode. In contrast to the bare $CuBi_2O_4$ photocathode (Figure S18) the protected $CuBi_2O_4/CdS/TiO_2/Pt$ photocathode (Figure 8a) shows nearly complete suppression of the dark current all the way down to the proton reduction potential of 0.0 V vs. RHE. This means the $CdS/TiO_2/Pt$ successfully protects the $CuBi_2O_4$ from fast corrosion. At 0.0 V vs. RHE the photocurrent density approaches -1.0 mA/cm^2.

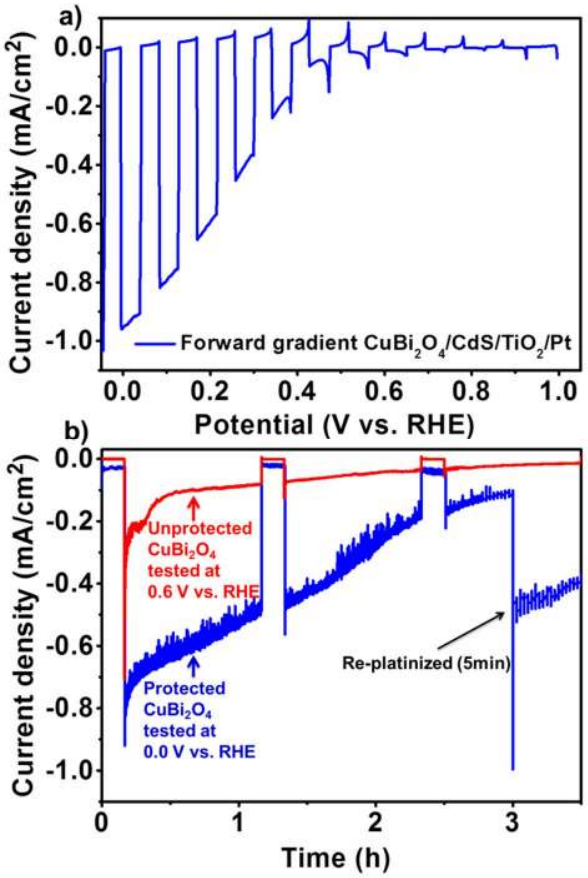

Figure 8. (a) Chopped LSV for a forward gradient $CuBi_2O_4/CdS/TiO_2/Pt$ photocathode, and (b) Constant potential measurements for an unprotected $CuBi_2O_4$ photocathode at 0.6 V vs. RHE (red line) and a forward gradient $CuBi_2O_4/CdS/TiO_2/Pt$ photocathode at 0.0 V vs. RHE (blue line). Measurements were done in 0.3 M K_2SO_4 and 0.2 M phosphate buffer (pH 6.65) with N_2 bubbling under front ($CuBi_2O_4/CdS/TiO_2/Pt$) and back ($CuBi_2O_4$) illumination.

To further assess the stability of the bare $CuBi_2O_4$ and protected $CuBi_2O_4/CdS/TiO_2/Pt$ photocathodes, and to prove H_2 production, their photocurrent densities were measured in pH neutral electrolyte with N_2 bubbling at a constant potential for several hours under periodically chopped illumination, as shown in Figure 8b. Even at a relatively positive potential of 0.6 V vs. RHE, the unprotected $CuBi_2O_4$ photocathode corrodes very fast, as indicated by the immediate decay of the red line and a decrease of 89 % in photocurrent density within 1 h. In contrast, the $CuBi_2O_4/CdS/TiO_2/Pt$ shows much improved stability, extending the lifetime of the photocathode from a few minutes to several hours. A significant portion of the decay is most likely due to gradual delamination of the Pt electrocatalyst instead of actual photocorrosion.[31] To test this, the photocathode was re-platinized briefly (5 min.) after 3 hours of operation, after which the photocurrent density was restored to more than half its initial value. These encouraging first results suggest that the forward gradient $CuBi_2O_4$ photocathodes can be further stabilized by optimizing the coverage of the protection layer and adhesion of the electrocatalyst.

We integrated the photocurrent density of the $CuBi_2O_4/CdS/TiO_2/Pt$ photocathode over time to obtain the total charge that was passed -3601 mC/cm² for the blue curve of Figure 8b). The obtained value is over 10 times larger than the total charge needed to reduce all cations including Cu^{2+}, Bi^{3+}, Cd^{2+}, and Ti^{4+} in the composite photocathode (-471 mC/cm²). Thus, at least 87 % of the photocurrent density went towards another photo-reduction reaction, most likely proton reduction. Furthermore, gas bubbles were visually observed on the photocathode surface during the measurement, as shown in Figure S20. In order to measure H_2 directly and calculate the Faradaic efficiency, differential electrochemical mass spectrometry (DEMS) measurements were performed on the $CuBi_2O_4/CdS/TiO_2/Pt$ photocathode. As shown in Figure S21, the current density and H_2 signal from the DEMS are well matched with the onset in H_2 production occurring around 0.4 V vs. RHE. When the $CuBi_2O_4/CdS/TiO_2/Pt$ photocathode was tested at a constant potential of 0.0 V vs. RHE for 1 h, it maintained a H_2 signal and a current signal of 0.030 nA and -62 μA, respectively, as shown in Figure S22. To calibrate the PEC cell the H_2 signal was measured vs. current for a Pt sheet as shown in Figure S23). Using equation (8) from the Experimental Section, this corresponds to a Faradaic efficiency ($\eta_{Faradaic}$) of 91 % for the H_2 evolution reaction.

CONCLUSIONS

We designed a simple two-step, diffusion-assisted spray pyrolysis process to introduce a concentration gradient of Cu vacancies in $CuBi_2O_4$. These vacancies act as acceptor dopants, and the resulting doping profile introduces an electric field (band bending) in the $CuBi_2O_4$ that significantly enhances the separation of the photo-generated charge carriers. Compared to homogeneous $CuBi_2O_4$ photocathodes, $CuBi_2O_4$ photocathodes with a forward gradient show highly improved charge separation efficiency and PEC performance, while a reverse gradient has a reduced charge separation efficiency PEC performance. At 0.6 V vs. RHE, with H_2O_2 as an electron scavenger, the forward gradient $CuBi_2O_4$ photocathodes produce record photocurrent densities for $CuBi_2O_4$ up to -2.5 mA/cm² under AM 1.5 simulated sunlight along with a charge separation efficiency of 34 % for 550 nm light. To test for H_2 production, $CuBi_2O_4$ photocathodes with a forward gradient were protected from photo-corrosion with a CdS/TiO_2 heterojunction layer and Pt was photodeposited as an electrocatalyst. The $CuBi_2O_4/CdS/TiO_2/Pt$ showed dramatically improved stability and H_2 was produced with a faradaic efficiency of ~91 % at 0.0 V vs. RHE. The gradient self-doping does not require the addition of external dopants and as a result the tetragonal crystal structure and intrinsic charge carrier mobility of $CuBi_2O_4$ are maintained. We hope this new concept of using forward gradient self-doping to improve charge separation can be applied to other multinary metal oxides as well.

EXPERIMENTAL

Material synthesis

A 40 mM Bi^{3+} precursor was prepared by dissolving $Bi(NO_3)_3 \cdot 5H_2O$ (98 %, Alfa Aesar) in a 1 : 9 mixture of acetic acid (≥ 99.8 %, Sigma Aldrich): ethanol (≥ 99.8 %, Sigma Aldrich). A 20 mM Cu^{2+} precursor was prepared by dissolving $Cu(NO_3)_2 \cdot 3H_2O$ (99-104 %, Sigma-Aldrich) in ethanol (≥ 99.8 %, Sigma Aldrich). The substrates were fluorine-doped tin oxide (FTO) coated glass (7 Ω/sq, Nippon Sheet Glass Co. Ltd.) for the PEC measurements, while fused silica ('quartz') substrates (H Baumbach & Co. Ltd) were used for the optical absorption and microwave conductivity measurements. Prior to deposition, the substrates were cleaned by three successive 15 min ultrasonication and rinsing steps in 1 vol % Triton in water, acetone, and ethanol, followed by drying under a stream of nitrogen. Before deposition was started the substrates were placed on the hot plate and heated to the preset temperature of 450 °C. The spray nozzle (Quickmist Air Atomizing Spray) was placed 20 cm above the heating plate and driven by an overpressure of 0.6 bar of nitrogen gas. Pulsed deposition mode was used, with one spray cycle consisting of 5 s spray time followed by a delay of 55 s to allow complete evaporation of the solvent and pyrolysis of any remaining organics.

Homogeneous $CuBi_2O_4$ films were prepared using the previously reported spray pyrolysis recipe with triethyl orthoformate (TEOF) and polyethylene glycol (PEG) as additives.[4] $CuBi_2O_4$ films with a forward gradient were prepared through a two-step diffusion-assisted spray pyrolysis process, which is illustrated in Figure 9. First the Bi^{3+} precursor was sprayed onto FTO substrate at a deposition temperature of 450 °C resulting in a yellow Bi_2O_3 film as confirmed by XRD. Next the Cu^{2+} precursor was sprayed successively on top of the Bi_2O_3 film at 450 °C, during which Cu diffuses into the Bi_2O_3. The high mobility and small size of Cu greatly facilitates the diffusion of Cu^{2+} into Bi_2O_3. $CuBi_2O_4$ photocathodes with forward gradient were obtained without any post annealing. Reverse gradient $CuBi_2O_4$ films were prepared by first spraying the Cu^{2+} precursor, followed by the Bi^{3+} precursor. This two-step process avoids the rapid hydrolysis of Bi^{3+}, which occurs when the $Bi^{3+}$and Cu^{2+} precursors are combined in acetic acid and ethanol; thus, TEOF and PEG additives are not required. Moreover, the growth rate is 2.7 nm/min, which is 3.3 times higher than that of our previous reported recipe.[4]

CdS/TiO_2 overlayers were deposited onto the forward gradient $CuBi_2O_4$ films using previously reported procedures.[30] The platinum electrocatalyst was photoelectron-deposited onto the $CuBi_2O_4/CdS/TiO_2$ from a solution containing 1 mM H_2PtCl_6 in 0.1 M Na_2SO_4, using a constant cathodic current of 25 μA/cm² for 10 min with constant illumination from a AM 1.5 solar simulator (LOT-Quantum Design GmbH). The photoelectrodeposition was performed in a two-electrode configuration with Pt mesh as a counter electrode.

Material Characterization

The morphology and the elemental distribution of the films were analyzed using a LEO GEMINI 1530 field emission scanning electron microscope (FESEM) with an energy dispersive X-ray fluorescence (EDX) spectrometer operated at an acceleration voltage of5 kV and 20 kV for SEM and EDX, respectively. The cross section elemental distribution of the $CuBi_2O_4$ films was determined by EDX mapping, where the Cu (K_α) and the Bi (M) peaks were used to calculate the Cu and Bi content, respectively. The crystal structures of the films were investigated with a Bruker AXS D8-Advance X-ray diffractometer with a Cu K_α radiation (λ = 0.154 nm) using glancing incidence X-ray diffraction (GIXRD) measurements. To determine the crystallite size, Scherrer analysis was performed as described in our previous paper.[4]

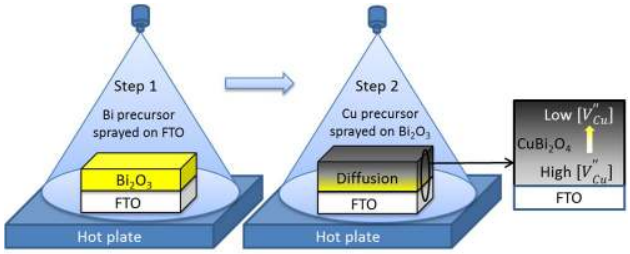

Figure 9. Schematic drawing of the two step deposition of $CuBi_2O_4$ with forward gradient.

The short-range structure and vibration modes were analyzed by Raman spectroscopy (Dilor micro LabRam, Horiba) with a laser excitation wavelength of 635 nm and a power of 0.6 mW at the objective (spot size: ~1 μm in diameter). The surface morphology was investigated by atomic force microscopy (AFM, Park System, XE-100) operated in tapping mode using an etched Si tip with a tip radius of 10 nm and a force constant of 40 N/m. All scans were performed on a scale of 5 μm × 5 μm with the lateral resolved height information on a square array of 256 × 256 pixels.

The charge carrier mobility and lifetime were investigated by time resolved microwave conductivity (TRMC) measurements. TRMC is a non-contact technique based on the measurement of the change of the microwave power reflected by a sample induced by a pulsed laser, as illustrated in Figure S24.[32-35] The X-band (8.2-12.4 GHz) microwaves are generated using a voltage controlled oscillator (SiversIMA VO3262X). To enhance the sensitivity, all measurements were performed in a cavity whose dimensions match the wavelength of the microwave. The resonance frequency of the cavity, loaded with the sample, was determined by measuring the reflected power as a function of the microwave frequency and normalized with respect to the power measured for a fully reflecting copper plate. From the resulting resonance curve the resonance frequency f_o, corresponding to minimum reflected power and maximum electric field strength within the cavity, was found to be 8521 MHz for our $CuBi_2O_4$ films. During the measurements, a change in the reflected microwave power upon sample excitation by 6 ns (full-width at half-maximum) pulses of a frequency-doubled Q-switched Nd:YAG laser at a wavelength of 532 nm (10 Hz repetition rate), $\Delta P/P$, was monitored and correlated to the photoinduced change in the conductance of the sample, ΔG, according to

$$\frac{\Delta P}{P}(t) = -K\Delta G(t) \qquad (1)$$

where K is the sensitivity factor derived from the resonance characteristics of the cavity and the dielectric properties of the medium.

From the measured change in the photoconductance, the product of the charge carrier generation yield (ϕ) and the sum of electron and hole mobilities ($\Sigma\mu$) can be obtained according to

$$\Phi \sum \mu = \frac{\Delta G}{I_0 \beta e F_A} \qquad (2)$$

where I_o is the incident intensity per pulse, e is the elementary charge, β is the width-to-height ratio of the inner dimensions of the cavity, and F_A is the fraction of incident photons absorbed within the sample. The F_A values ranged from 0.56 to 0.61 at a wavelength of 532 nm, determined from transflectance measurements with a double-beam spectrometer Lambda 950 (Perkin-Elmer). The maximum sum-up charge carrier mobility was obtained from the peak signal and the carrier lifetime constants were deduced from the decay of the curve.

The charge carrier diffusion lengths (L_D) were calculated from the following formula,

$$L_D = \sqrt{\left(\frac{\mu k T}{e}\right)\tau} \qquad (3)$$

where μ is mobility ($m^2V^{-1}s^{-1}$), k is the Boltzmann constant, T is the temperature (K), e is the electronic charge (C), and τ is the charge carrier lifetime (s).The laser pulse intensity was 4.9×10^{14} photons cm^{-2} for all measurements.

Electrochemical and Photoelectrochemical Measurements

The photoelectrochemical measurements were carried out with an EG & G Princeton Applied Research 273 A potentiostat using a three-electrode configuration, with the $CuBi_2O_4$ film as the working electrode, an Ag/AgCl (saturated KCl) reference electrode, and a platinum wire counter electrode in a quartz-windowed PEC cell. A WACOM Class AAA solar simulator (WXS-50S-5H) was used as an illumination source (AM 1.5, 100 mW/cm^2). 0.3 M K_2SO_4 with 0.2 M phosphate buffer (pH 6.65) was used as an electrolyte with or without H_2O_2 added as an electron scavenger. The pH value was measured with a pH meter (OAKTON). All potentials were converted to the reversible hydrogen electrode (RHE) scale using the Nernstian relation,

$$V_{RHE} = V_{Ag/AgCl} + 0.059 \times pH + 0.197\ (V) \quad (4)$$

Monochromatic photocurrents were measured with a 300 W quartz xenon lamp coupled into a grating monochromator (Acton SpectraPro 150 i). An electronic shutter (Uniblitz LS6) was used, and a long-pass colored glass filter (Schott, 3 mm thick) was placed between the monochromator and the sample to remove second-order diffracted light. The shutter was actuated every 10 seconds, and the currents were determined first waiting for 8 s, following by averaging the measured values for 2 s before the shutter was actuated again. A dark and light measurement was taken for each data point, with 1.5 nm wavelength steps between each point.

IPCE was calculated using the following formula,

$$IPCE(\%) = \frac{J_{pho}(\lambda)}{P(W)} \times \frac{1240}{\lambda(nm)} \times 100 \qquad (5)$$

where J_{pho} is the photocurrent, P is the power, and λ is the wavelength. The APCE was calculated from the following formula,

$$APCE\ (\%) = \frac{IPCE\ (\%)}{A} \qquad (6)$$

where A is the absorptance. The IPCE of the $CuBi_2O_4$ photocathodes were measured at 0.6 V vs. RHE with H_2O_2 added.

Electrical impedance spectroscopy (EIS) and Mott–Schottky measurements were performed using a VersaSTAT 3 Potentiostat (AMETEK Co., Ltd.). Mott–Schottky plots were created based on the following formula,[36]

$$\frac{1}{C^2} = \frac{2}{e\,\varepsilon\,\varepsilon_0\,N_A}\left(-\varphi + \varphi_{fb} - \frac{k T}{e}\right) \qquad (7)$$

where C is the capacitance per unit area (F/m^2), ε is the relative permittivity (dielectric constant), ε_o is the permittivity of free space, N_A is the acceptor density, and φ_{fb} is the flat-band potential. AFM was used to estimate the real surface area from the geometric surface area of the working electrode in the PEC cell (i.e., our $CuBi_2O_4$ photocathode). The ε of $CuBi_2O_4$ is expected to vary with Cu/Bi ratio and frequency but there are limited reports in the literature. For bismuth cuprate glasses, it was shown that ε varies with the Cu/Bi ratio and frequency,

which can be modeled using the Cole-Cole equation.[37-38] Therefore we used this technique to estimate ε for various $CuBi_2O_4$ films and frequencies as shown in Figure S25 and described in the Supporting Information.

The photoelectrochemical stabilities of the $CuBi_2O_4$ and $CuBi_2O_4$/CdS/TiO_2/Pt photocathodes were tested in a three-electrode configuration using a BioLogic SP-200 potentiostat with illumination from a AM 1.5 solar simulator (LOT-QuantumDesign GmbH). The reference electrode was Ag/AgCl (saturated KCl) and a Pt mesh was used as the counter electrode. The sample was placed in a quartz-windowed PEC cell equipped with an O-ring to fix the area to 0.28 cm^2. A solution of 0.3 M K_2SO_4 with 0.2 M phosphate buffer (pH 6.65) was used as an electrolyte with N_2 bubbling during the measurement.

For H_2 detection, differential electrochemical mass spectrometry (DEMS) measurements were carried in a PEC cell with a thin electrolyte layer (~100 μm) between the $CuBi_2O_4$/CdS/TiO_2/Pt photocathode and a gas permeable membrane (ethylene-tetrafluoroethylene copolymer, Scimat) as shown in Figure S26. The photocathode was illuminated from the backside using a 150 W Xe lamp with an AM 1.5 G filter. The light power was adjusted to approximately 650 mW/cm^2 for light wavelengths between 400 and 900 nm. The gas permeable membrane acted as an inlet to the first vacuum chamber of a dually pumped vacuum system. A variable leak valve connected the first chamber to the second high vacuum chamber, which housed the quadrupole mass spectrometer (Pfeiffer Vacuum, QMG 220 M1). The DEMS cell design was closed with stagnant electrolyte so all gaseous or volatile compounds formed by the photocathode were collected through the permeable membrane and detected by the mass spectrometer. Two small holes in the electrolyte channel allowed for filling of the cell and insertion of the Ag/AgCl reference electrode and Pt wire counter electrode. To calibrate the PEC cell the H_2 signal was measured vs. current for a Pt sheet (see Figure S22 in the Supporting Information). Then the Faradaic efficiency for the photocathode could be calculate using the following equation, under the assumption that the Pt sheet has 100 % Faradaic efficiency for the H_2 evolution reaction,

$$\eta_{\text{faradaic}} = \frac{H_2 \text{ signal from photocathode}}{H_2 \text{ signal from Pt sheet}} \qquad (8)$$

After each DEMS measurement the electrolyte was exchanged to avoid undesired shifts in the pH.

ASSOCIATED CONTENT

Supporting Information

Electronic Supplementary Information (ESI) available: LSV scans, XRD pattern, IPCE spectra, EDX mapping, Mott-Schottky plots, AFM images, TRMC spectra.
This material is available free of charge via the Internet at http://pubs.acs.org.

AUTHOR INFORMATION

Corresponding Author

*sean.berglund@helmholtz-berlin.de

Author Contributions

The manuscript was written through contributions of all authors. All authors have given approval to the final version of the manuscript.

Notes

The authors declare no competing financial interest.

ACKNOWLEDGMENT

Fuxian Wang thanks the Oversea Study Program of the Guangzhou Elite Project (GEP JY201308, Guangzhou, China) for financial support. Part of this work is supported by the German Bundesministerium für Bildung and Forschung (BMBF), project "MeOx4H2" (03SF0478A). The University of Zurich, the University Research Priority Program (URPP) LightChEC, and the Swiss National Science foundation (AP Energy Grant # PYAPP2 160586) are gratefully acknowledged for financial support. Discussion with Dr. Yimeng Ma helped in the interpretation of our results.

ABBREVIATIONS

PEC, photoelectrochemical; FTO, fluorine-doped tin oxide; XRD, X-ray diffraction; SEM, scanning electron microscopy; AFM, atomic force microscope; LSV, linear sweep voltammetry; TRMC, time-resolved microwave conductivity; IPCE, incident-photon-to-current conversion efficiency; APCE, absorbed-photon-to-current conversion efficiency.

REFERENCES

(1) Arai, T.; Konishi, Y.; Iwasaki, Y.; Sugihara, H.; Sayama, K. *J. Comb. Chem.* **2007,** *9* (4), 574-581.

(2) Hahn, N. T.; Holmberg, V. C.; Korgel, B. A.; Mullins, C. B. *J. Phys. Chem. C.* **2012,** *116* (10), 6459-6466.
(3) Berglund, S. P.; Abdi, F. F.; Bogdanoff, P.; Chemseddine, A.; Friedrich, D.; van de Krol, R. *Chem. Mater.* **2016,** *28* (12), 4231-4242.
(4) Wang, F.; Chemseddine, A.; Abdi, F.; van de Krol, R.; Berglund, S. P. *J. Mater. Chem. A.* **2017,** 5, 12838-12847.
(5) Patil, R.; Kelkar, S.; Naphade, R.; Ogale, S. *J. Mater. Chem. A.* **2014,** *2* (10), 3661-3668.
(6) Sharma, G.; Zhao, Z.; Sarker, P.; Nail, B. A.; Wang, J.; Huda, M. N.; Osterloh, F. E. *J. Mater. Chem. A.* **2016,** *4*, 2936-2942.
(7) Park, H. S.; Lee, C.-Y.; Reisner, E. *Phys. Chem. Chem. Phys.* **2014,** *16* (41), 22462-22465.
(8) Chen, Z.; Jaramillo, T. F.; Deutsch, T. G.; Kleiman-Shwarsctein, A.; Forman, A. J.; Gaillard, N.; Garland, R.; Takanabe, K.; Heske, C.; Sunkara, M. *J. Mater. Res.* **2010,** *25* (01), 3-16.
(9) Kang, D.; Hill, J. C.; Park, Y.; Choi, K.-S. *Chem. Mater.* **2016,** *28* (12), 4331-4340.
(10) Hong, S. J.; Lee, S.; Jang, J. S.; Lee, J. S. *Energy Environ Sci.* **2011,** *4* (5), 1781-1787.
(11) Saito, R.; Miseki, Y.; Sayama, K. *Chem. Commun.* **2012,** *48* (32), 3833-3835.
(12) Zhang, K.; Shi, X.-J.; Kim, J. K.; Park, J. H. *Phys. Chem. Chem. Phys.* **2012,** *14* (31), 11119-11124.
(13) Saad, M.; Kassis, A. *Sol. Energy Mater. Sol. Cells.* **2003,** *79* (4), 507-517.
(14) Abdi, F. F.; Han, L.; Smets, A. H.; Zeman, M.; Dam, B.; van de Krol, R. *Nat. Commun.* **2013,** *4*, 2195.
(15) Abdi, F. F.; Savenije, T. J.; May, M. M.; Dam, B.; van de Krol, R. *J. Phys. Chem. Lett.* **2013,** *4* (16), 2752-2757.
(16) Ziwritsch, M.; Müller, S. n.; Hempel, H.; Unold, T.; Abdi, F. F.; van de Krol, R.; Friedrich, D.; Eichberger, R. *ACS Energy Lett.* **2016,** *1* (5), 888-894.
(17) Cao, D.; Nasori, N.; Wang, Z.; Mi, Y.; Wen, L.; Yang, Y.; Qu, S.; Wang, Z.; Lei, Y. *J. Mater. Chem. A.* **2016,** *4*, 8995-9001.
(18) Anderman, M.; Kennedy, J. H. *J. Electrochem. Soc.* **1984,** *131* (1), 21-26.
(19) Hardee, K. L.; Bard, A. J. *J. Electrochem. Soc.* **1977,** *124* (2), 215-224.
(20) Li, J.; Peter, L. *J. Electroanal. Chem. Interfacial Electrochem.* **1985,** *182* (2), 399-411.
(21) Ghose, J.; Kanungo, A. *J. Therm. Anal. Calorim.* **1981,** *20* (2), 459-462.
(22) Popović, Z. V.; Kliche, G.; Cardona, M.; Liu, R. *Phys. Rev. B.* **1990,** *41* (6), 3824-3828.
(23) Yuvaraj, S.; Karthikeyan, K.; Kalpana, D.; Lee, Y. S.; Selvan, R. K. *J. Colloid Interface Sci.* **2016,** *469*, 47-56.
(24) Hagemann, H.; Bill, H.; Walker, E.; François, M. *Solid State Commun.* **1990,** *73* (6), 447-451.
(25) Kelly, J.; Vanmaekelbergh, D. *Electrochim. Acta.* **1998,** *43* (19), 2773-2780.
(26) Abdi, F. F.; Berglund, S. P. *J. Phys. D: Appl. Phys.* **2017,** 50 (19), 193002.
(27) Paracchino, A.; Mathews, N.; Hisatomi, T.; Stefik, M.; Tilley, S. D.; Grätzel, M. *Energy Environ Sci.* **2012,** 5 (9), 8673-8681.
(28) Seger, B.; Tilley, D. S.; Pedersen, T.; Vesborg, P. C.; Hansen, O.; Grätzel, M.; Chorkendorff, I. *Rsc Advances.* **2013,** *3* (48), 25902-25907.
(29) Choi, J.; Song, J. T.; Jang, H. S.; Choi, M.-J.; Sim, D. M.; Yim, S.; Lim, H.; Jung, Y. S.; Oh, J. *ELECTRON MATER LETT.* **2017,** *13* (1), 57-65.
(30) Septina, W.; Prabhakar, R. R.; Wick, R.; Moehl, T.; Tilley, S. D. *Chem. Mater.* **2017,** *29* (4), 1735-1743.
(31) Shao-Horn, Y.; Sheng, W.; Chen, S.; Ferreira, P.; Holby, E.; Morgan, D. *Top. Catal.* **2007,** *46* (3), 285-305.
(32) Kroeze, J. E.; Savenije, T. J.; Warman, J. M. *J. Am. Chem. Soc.* **2004,** *126* (24), 7608-7618.
(33) Kunst, M.; Beck, G. *J. Appl. Phys.* **1986,** *60* (10), 3558-3566.
(34) Savenije, T. J.; Ferguson, A. J.; Kopidakis, N.; Rumbles, G. *J. Phys. Chem. C.* **2013,** *117* (46), 24085-24103.
(35) Infelta, P. P.; De Haas, M. P.; Warman, J. M. *Radiat. Phys. Chem.* **1977,** *10* (5-6), 353-365.
(36) Gomes, W.; Vanmaekelbergh, D. *Electrochim. Acta.* **1996,** *41* (7-8), 967-973.
(37) Hazra, S.; Ghosh, A. *J. Appl. Phys.* **1998,** *84* (2), 987-992.
(38) Cole, K. S.; Cole, R. H. *J. Chem. Phys.* **1941,** *9* (4), 341-351.

Table of Contents